Millimeter-Wave Channel Measurement and Modeling: A NIST Perspective

Camillo Gentile, Peter B. Papazian, Nada Golmie, Kate A. Remley, Peter Vouras, Jelena Senic, Jian Wang, Derek Caudill, Chiehping Lai, Ruoyu Sun, and Jack Chuang

The authors provide an overview of mmWave channel sounding through three types of systems: switched array, virtual array, and phased array, at 28 GHz, 60 GHz, and 83 GHz. They describe how mmWave channel models, for path loss, dispersion, multipath tracking, Doppler spread, and blockage, differ from sub-6-GHz models, substantiated by some recent results.

ABSTRACT

The exponential increase in wireless data transmission from smartphones has led to the saturation of the sub-6-GHz bands — where cellular networks have operated to date — forcing providers to migrate to the millimeter-wave (mmWave) regime for 5G. Although available channel bandwidths will grow from tens of megahertz to several gigahertz, propagation loss will be substantially higher. To compensate the link budget, phased array antennas with 20 dBi–40-dBi gain will be employed at the base and mobile stations. Since beamwidth is inversely proportional to gain, the resultant pencilbeams will be only 3°–15° wide and thus must be electronically steered to ensure that they are aligned between the stations. The high directionality of 5G systems will fundamentally change channel propagation models and channel sounding systems and techniques used to measure the model properties. The National Institute of Standards and Technology is on the forefront of defining that change. In this article, we provide an overview of mmWave channel sounding through three types of systems: switched array, virtual array, and phased array, at 28 GHz, 60 GHz, and 83 GHz. In addition, we describe how mmWave channel models, for path loss, dispersion, multipath tracking, Doppler spread, and blockage, differ from sub-6-GHz models, substantiated by some of our most recent results.

INTRODUCTION

The saturation of the sub-6-GHz bands — where cellular networks including fourth generation (4G) have operated to date — due to wireless data transmission from smartphones prompted the Federal Communications Commission (FCC) in July 2016 to release nearly 11 GHz of spectrum in the 28 GHz–73 GHz millimeter-wave (mmWave) band for 5G communications. Although free-space and penetration loss (and oxygen absorption loss around 60 GHz) are notably greater, the bandwidth available per channel will grow from 10 MHz to 1 GHz and beyond.

The real game changer for 5G has been the development of mmWave phased array antennas [1]. The arrays feature tens to hundreds of antenna elements on each board. By phasing the elements — a technique known as beamforming — their individual patterns combine constructively to generate a beam with 20 dBi–40-dBi gain. The joint gain from the base and mobile stations compensates the link budget for the higher propagation loss, enabling connectivity to hundreds of meters. Since beamwidth is inversely proportional to gain, the resultant pencil beams will be only 3°–15° wide and thus must be electronically steered to ensure that they are aligned between the stations. In non-line of sight (NLoS) conditions or in the event of blockage by humans, vehicles, and so on, the direct propagation path between the stations will be severely attenuated [2]. The beams must then be redirected toward other dominant (strong) paths reflected from ambient objects to maintain connectivity. Even if the direct path is clear, these paths will be exploited — along which multiple streams of data will be sent — for spatial multiple-input multiple-output (MIMO) in order to boost throughput or feed multiple users. Polarization MIMO, in which two orthogonal streams are sent along the same path with slant polarizations, will also be implemented.

Pencil beams act as spatial filters, naturally suppressing potential interferers to deliver signal-to-interference-plus-noise ratios (SINRs) unseen to date, which will enable modulation schemes up to 1024-quadrature amplitude modulation (QAM). Coupled with ultra-wide channel bandwidths, channel bonding — consolidating individual channels to increase instantaneous bandwidth to several gigahertz — and spatial/polarization MIMO, throughput will approach hundreds of gigabits per second for new applications such as wireless streaming of ultra-high-definition (UHD) video and vehicle-to-vehicle (V2V) communications [3]. Measured data that captures the channel properties relevant to these 5G techniques are thus needed to develop meaningful models on which component and system development can be based; simply extrapolating current sub-6-GHz models to mmWave frequencies is insufficient. Accordingly, some looming questions for 5G are:

• How big are the differences in propagation characteristics across the mmWave band? The difference in wavelength between 30 GHz and 90 GHz — six decades in frequency — is just 1.6 mm, so highly precise calibrated equipment needs to be provided.
• What is the strength of the paths in both polarizations, and is orthogonality maintained during transmission?

- How many dominant paths are available in an environment? This value maps to the maximum number of independent data streams that can be sent.
- What is the distribution of the paths in space? It is important to know how close they are to avoid mutual interference between beams and within beams.
- Given a fixed number of phased array elements, how does one partition the elements? Does one allocate all elements to synthesize a single high-gain beam along one path or split them into wider, lower-gain beams across multiple paths? Or, rather than generating multiple beams, is it more advantageous to allocate elements to create nulls along the directions of potential interferers, increasing the SINR?
- How do the channel properties evolve over time? This is critical since 5G systems will track beams to reduce how often the channel has to be estimated.

The 5G mmWave Channel Model Alliance [4] — an international alliance of companies, universities and government institutions, including the National Institute of Standards and Technology (NIST) — was formed in 2015 to support the development of more accurate, consistent, and predictive channel models. In this article, we touch upon some answers that have been provided by NIST and other members of the Alliance thus far. The remainder of this article is divided into two main sections: the first on channel measurement systems and the second on models derived from the ensuing measurements.

CHANNEL MEASUREMENT

In this section, we describe three types of channel sounders that NIST currently has to measure the channel model parameters relevant to 5G mmWave systems.

The power detected by a receiver (RX) can be modeled as a train of N plane waves, each representing a distinct propagation path from the transmitter (TX). Let n index each path, characterized by propagation delay, τ_n, and complex amplitude, a_n, accounting for attenuation and any phase shift due to reflection from ambient objects. A path is also characterized by its angle of departure (AoD) from the TX and its angle of arrival (AoA) to the RX, denoted conveniently as a *double-directional angle* $\boldsymbol{\theta}_n = [\theta_n^{AoD,A}, \theta_n^{AoD,E}, \theta_n^{AoA,A}, \theta_n^{AoA,E}]$, where A and E denote azimuth and elevation, respectively, in the 3D space of the antennas. Finally, each path has a Doppler frequency shift, Δf_n, which quantifies how quickly the channel changes in time, t. The *time-variant double-directional channel impulse response* at baseband can be written compactly as

$$h(t,\tau,\boldsymbol{\theta}) = \sum_{n=1}^{N} a_n e^{j2\pi\Delta f_n t} \cdot \delta(\tau - \tau_n, \boldsymbol{\theta} - \boldsymbol{\theta}_n). \qquad (1)$$

The basic task of radio frequency channel sounding is to characterize the parameters of each path in Eq. 1. The complex amplitude vs. delay can be measured through correlation-based techniques, such as the one described later. The advantage of these techniques is that the channel can be sampled very rapidly — within the period
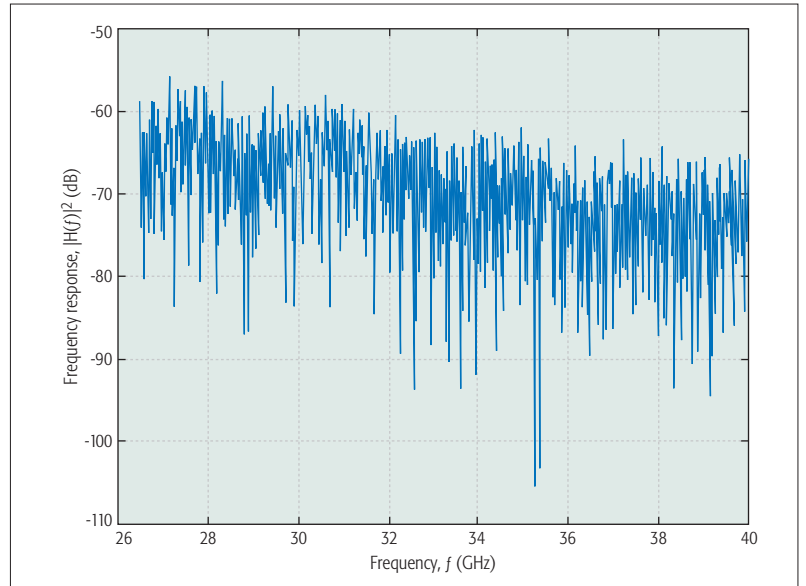

Figure 1. Channel frequency response from 26.5 GHz–40 GHz measured in our lab with a vector network analyzer. The power of the combined paths varied up to 42 dB across the band.

the channel is constant, otherwise known as the *coherence time* — and thus are suited for mobile scenarios.

Alternatively, the channel response can be measured in the frequency domain with a vector network analyzer and then transformed to the delay domain through the inverse Fourier transform. VNAs can span an extremely large frequency range. For example, Fig. 1 shows the frequency response of a channel, $H(t_0, f, \boldsymbol{\theta}_0)$ — Eq. 1 transformed from the delay to the frequency domain for a given t_0 and $\boldsymbol{\theta}_0$ measured in our lab between 26.5 GHz–40 GHz. The power of the combined paths varied up to 42 dB across the band; hence, while the frequency dependence of the complex amplitude, $a_n(f)$, could be neglected with 4G channel bandwidths on the order of tens of megahertz, this is no longer the case with 5G bandwidths up to 8.64 GHz [3]. These sorts of high-precision measurements are useful in characterizing this dependence. However, due to the VNA acquisition times on the order of seconds, they are only suited for static scenarios or ones with very low mobility.

The complex amplitude is also polarization dependent, so the sounder antennas should be both vertically and horizontally polarized. Because paths can become depolarized upon reflection, it is important to quantify cross-polarization discrimination (orthogonality). In [5], the discrimination factor at 73 GHz ranged between 11.7 dB–12.8 dB for specific wall materials such as brick and wooden panels, but was reported as low as 7.5 dB for other objects. Comparable values at the same frequency were reported in [6], however for the office environment as a whole rather than for specific materials: in NLoS, the factor ranged between 12.9 dB–16.5 dB and, as expected, improved in line of sight (LoS) to 21.4 dB–23.8 dB since the dominance of the direct path will bias the results toward the inherent cross-polarization separation of the antennas, which is typically around 40 dB. At 28 GHz [6], the factor dropped
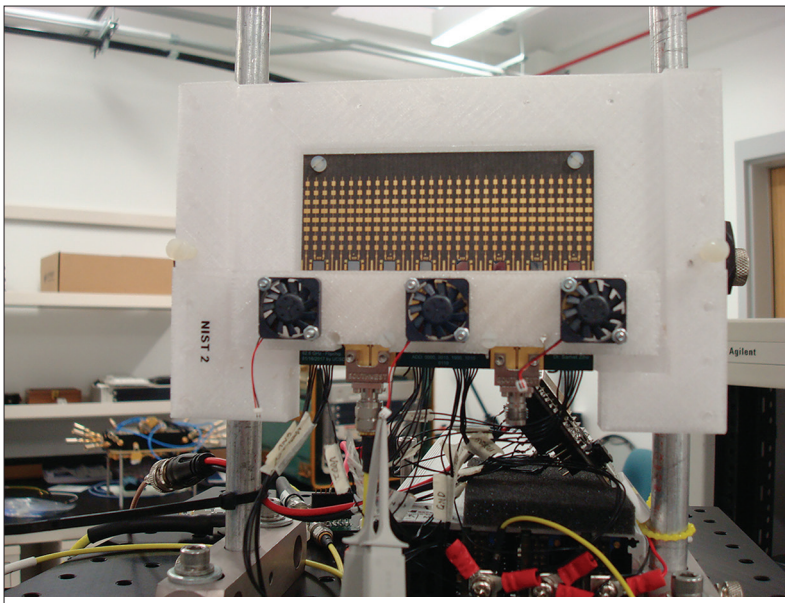
Figure 2. 8 × 32 60-GHz phased array antenna mounted on a rotator in our lab. The elements are spaced at half-wavelength, so the array dimensions are only 4 cm × 16 cm.

relation is done in post-processing. This means that the channel can be sampled at Δt, corresponding to a maximum measurable Doppler shift of 1.9 MHz. Thus, scenarios up to a closing speed of 34 km/h can be handled when investigating V2V scenarios.

The AoA of each path is determined by comparing its delay across the RX array elements: as the plane wave approaches, its arrival angle will be closest (farthest) to the boresight angle of the element that detects the path first (last). Based on this principle, any angle in between can be interpolated. The principle is the same for the AoD at the TX array. The azimuth and elevation of the AoD and AoA were validated with a mean error of 2.1° [9]. Our data can also be used for generating the directional channel impulse response of other systems by appropriately applying the system antenna patterns.

Our 28-GHz and 83-GHz switched array channel sounders are almost identical to the 60-GHz sounder.

VIRTUAL ARRAY CHANNEL SOUNDER

To report channel parameters with greater precision, we transferred the RX-array mount from the robot onto a 2D positioner. The positioner sequentially translates the switched array antenna structure across a regularly spaced grid of 30 × 30 points through mechanical scanning in the horizontal plane. Because our RX array has 16 horn antennas, the system is equivalent to 16 virtual planar arrays, each with the limited FoV corresponding to a single horn, but collectively has the same broad FoV of the switched array system. However, there are three important advantages:
1. The points are spaced at half-wavelength,[1] so coherent combination in complex amplitude is possible. Accordingly, the inherent 22.5° beamwidth of the horns is collapsed to a 3.8° pencil beam that can be steered in any direction within the FoV of the horn.
2. The 18.1 dBi gain of the horns multiplied by the directivity of the array factor provides for a virtual array gain of 47.6 dBi.
3. Each point of the virtual array is digitized separately, enabling the use of advanced super-resolution techniques.

Some results from the virtual array are described later.

PHASED ARRAY CHANNEL SOUNDER

While our virtual array channel sounder enables a very high degree of precision in parameter estimation, it is slow, as mentioned earlier: a channel sweep requires 44 min, so only static environments can be characterized. To meld the speed of the switched array system with the precision of gridded elements, our next generation of channel sounders implements real phased array antennas. Figure 2 shows a picture of our 8 × 32 60-GHz phased array. While slower than the switched array, it is steerable and its beamwidth is tunable, with nominal 3.6° beamwidth and 28-dBi gain. Each board can scan 90° in azimuth and hence enable an omni view; we will have 4 boards arranged at right angles with respect to each other at both the RX and TX. The beam pattern can be switched at a rate of 30 MHz, so a full RX-TX sweep in azimuth requires 0.33 s. We

decisively to 8.7 dB–11.0 dB in NLoS and 13.3 dB–14.6 dB in LoS.

To measure double-directional angle, the most common approach is to equip the system with directional horn antennas [7]. The AoD and AoA are swept through mechanical rotation to get a different channel response for each pair of look angles. The angular resolution, however, is limited to the beamwidth of the antennas, which is typically 10° to 20°. Virtual arrays [8], such as the one described later, mechanically translate the antennas on a positioner to enable *super-resolution* — resolution beyond the inherent beamwidth of the antennas — on the order of degrees. The problem with mechanical rotation/scanning is that it is notoriously slow, and a single channel acquisition can take up to six hours, limiting measurement campaigns to static environments. On the contrary, electronically switched arrays, as described in the next section, can be very fast.

SWITCHED ARRAY CHANNEL SOUNDER

The TX of our switched array 60-GHz channel sounder [9] is mounted on a tripod and the untethered RX on a mobile robot. The RX features a circular array of 16 horn antennas, each with 18.1 dBi gain and 22.5° beamwidth. The resultant azimuthal field of view (FoV) of the array is omnidirectional, while its elevational FoV is 45°. The TX array is a replica of the RX array, but with only 8 elements, restricting its azimuthal FoV to 180°.

The TX generates a pseudorandom-noise (PN) code with 0.5 ns chip length, or equivalent 2 GHz bandwidth. The code is upconverted to 60.5 GHz center frequency and electronically switched through the 128 (16 × 8) RX-TX antenna pairs, requiring only $\Delta t = 262$ µs for a full channel sweep. At the RX, the received signal is downconverted and then directly digitized. For each antenna pair, the digitized signal is correlated with the known code, yielding a train of pulses, each corresponding to a distinct path. The advantage of direct digitization is that the cor-

---

[1] Equivalent to the Nyquist sampling rate in the spatial domain.

have a similar phased array at 28 GHz that has separate feeds for both polarizations [1].

CHANNEL MODELING

This section explains the most important aspects of channel models with the intent of highlighting how mmWave channel properties differ from sub-6-GHz.

PATH LOSS MODELS

Path loss models are useful for link-layer analysis. They describe how the total received power — the *path gain* (squared amplitude) over all N detected paths — decays with the parameters of the RX-TX configuration. Accordingly, the normalized[2] path loss per configuration is computed as

$$PL = 1 / \sqrt{\sum_{n=1}^{N} |a_n|^2}. \qquad (2)$$

The model itself is written as a function, $PL(d, f_c, h_B)$, where the RX-TX distance (d) (large-scale distance over many orders of wavelength), center frequency, and base station height (h_B) are the most typical configuration parameters.

Beamwidth-Dependent Models: Legacy cellular systems including 4G employ omnidirectional antennas at the mobile station. That is why most path loss models to date are based on the received power over paths from all directions (Eq. 2). In reality, 5G transceivers will steer their pencil beams toward the dominant channel paths, and the properties of the strongest detected path in particular may differ significantly from those of the omni model, most notably in NLoS. In NLoS conditions, since the direct path is severely attenuated, most of the power stems from secondary paths, which may be comparable in strength. Hence, the strongest detected path will represent only a fraction of the total power available. For example, from the same measurements in [2], the path loss exponent — the rate at which the signal fades over distance — is 6.19 for the strongest detected path[3] but only 4.81 for the omni model in NLoS, whereas in LoS they are almost identical: 1.90 and 1.93, respectively. (The theoretical value in free-space is 2.0.).

Of course, real phased-array antennas have finite beamwidth — inversely proportional to the center frequency and the array dimensions [1] — and hence will admit more than the strongest path alone: The beam acts as a spatial filter and as its width increases, more and more paths will be admitted, collapsing to the omni model at the extreme. Thus, to make models truly useful for 5G systems, they should be beamwidth dependent. Beamwidth-dependent models can be extended beyond focus on the strongest path alone to secondary paths as well. Models for the latter will apply when the former is blocked and/or for spatial MIMO. Omni models are still relevant to 5G because beamforming training — the process in which the channel is estimated to determine the double-directional angle of the dominant paths — will be carried out with an omni pattern at the most robust (slowest data rate) modulation scheme. Once the angles are found, however, beamwidth-dependent models are more accurate to determine the fastest modulation scheme attainable.

Wide-Sense Stationarity: Path loss models used widely in 4G are referred to as wide-sense stationary because they are independent of the specific RX-TX configurations. To guarantee stationarity, measurements are taken over a large ensemble of configurations to marginalize the site-specific characteristics. However, this will often lead to much larger fit error than what would otherwise be witnessed using a single TX alone. And since link distances will be much shorter than at sub-6-GHz, path loss will be more localized to the TX/base station, justifying site-specific models.

Another property that renders mmWave path loss models site specific is that the direct path will effectively be lost in the transition between LoS and NLoS due to high penetration loss. The transition constitutes a discontinuity or breakpoint distance in the model, at which the path loss exponent can change drastically, as pointed out earlier. Because the discontinuity is site specific, the model is no longer wide-sense stationary. To reconcile the enhanced accuracy of breakpoint models with the general applicability of wide-sense stationary models, a floating breakpoint model is proposed in [2]. The model is "floating" because it is rendered independent of the actual discontinuities in the measurement campaign, so the breakpoint(s) itself becomes a model parameter.

Generally speaking, high penetration loss makes the waveguiding of reflected paths along the structural confines of an environment a natural propagation mechanism in NLoS. And based on the waveguiding effect, a model may in fact have multiple breakpoints. This is especially true indoors in the office environment with corridors, confined spaces, and staircases; this is also true outdoors in urban canyons and tunnels, and even in residential areas if the base height is low enough — such as on rooftops, as envisioned for 5G last-mile deployment. In such cases, the distance parameter no longer obeys the Euclidean metric, but rather the metric along the waveguide. In [2], it is shown that the correlation coefficient between path loss and distance in a corridor improves from −0.49 to 0.95 when the metric is modified from Euclidean to waveguide. In other work in an urban canyon environment [10], modeling the distance along the waveguide reduces the fit error from roughly 15 dB to 2 dB.

DISPERSION MODELS

Whereas path loss models represent how the total power detected by the receiver varies with the RX-TX configuration, dispersion models represent how the power is distributed in the delay-angle (τ-θ) space over all paths per configuration, enabling the complete reconstruction of the channel response in Eq. 1. Besides characterizing path distribution in angle for MIMO, dispersion models are used for filter design in the delay domain (channel equalization) and to characterize small-scale fading: the variation in complex amplitude over tens of wavelengths due to constructive/destructive interference between paths.

The source of small-scaling fading for 5G is very different than for its predecessors. At lower frequencies, the channel is rich in multipath due to the presence of both reflection and diffrac-

The angle-of-arrival of each path is determined by comparing its delay across the RX-array elements: as the plane wave approaches, its arrival angle will be closest (farthest) to the boresight angle of the element that detects the path first (last). Based on this principle, any angle in between can be interpolated.

[2] Assumes unity transmission power and antennas gains.

[3] While the actual antenna beamwidth of the system is 45°, the strongest detected path was extracted individually from the other channel paths using super-resolution techniques.

[4] However it may occur that multiple specular paths originating from flat surfaces in close proximity are clustered together.
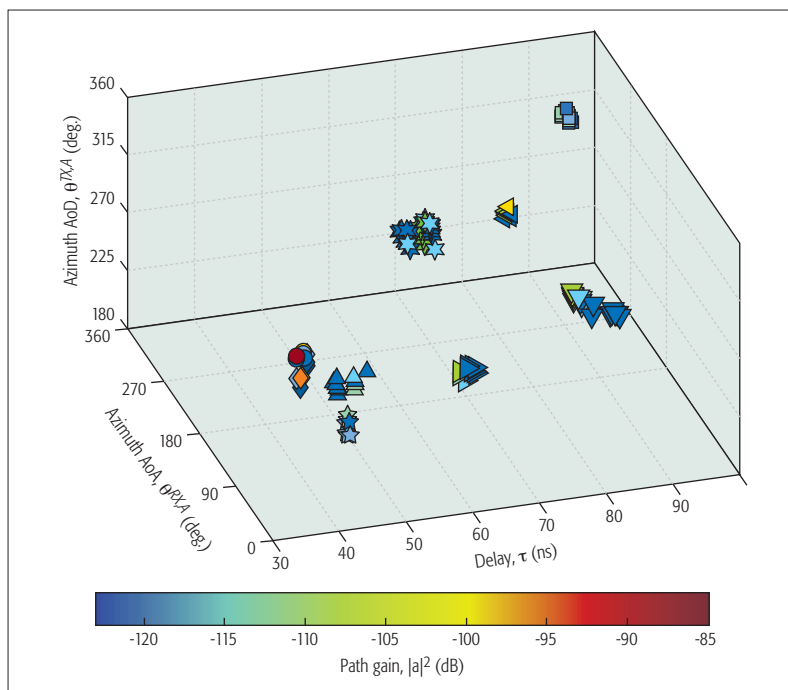
Figure 3. Clustered paths in the delay-AoD-AoA space (elevation omitted) measured with our 60-GHz switched array sounder in a data center. Each cluster is displayed with a different symbol, and each path is color-coded against path gain. For most clusters, the strongest specular component is evident, while the weaker ones are diffuse components.

tion. In addition, the omni antenna at the mobile station will capture all paths, multiplying interference. Finally, the ability to resolve individual paths is diminished as bandwidths are three orders of magnitude less than for 5G. On the contrary, at mmWave high penetration loss and lack of diffraction — demonstrated to be 15 dB–20 dB weaker than reflection [2, 11] — render the channel "sparse." Rather, *diffuse reflections* from surface roughness must now be accounted for since the roughness is comparable in size to the wavelength. Weak diffuse reflections cluster around strong *specular reflection*s — reflections from flat surfaces — in the delay-angle space, so when the transceivers steer their beams toward the specular components, they will inevitably detect diffuse components as well, giving rise to fading. The severity of the fade will depend on the relative power of the specular component with respect to the composite power of the diffuse components, gauged by the Ricean K-factor of the cluster. The severity will also depend on the angular spread of the diffuse components within the clusters: the closer in angle they are to the specular component, the greater they will be weighted by the beam pattern. Cluster angular spread will also dictate any potential inter-beam interference.

The IEEE 802.11ay Task Group as well as other industry consortia (MiWEBA, METIS, mmMAGIC) have subscribed to map-based dispersion models for mmWave systems [12]. They are often referred to as quasi-deterministic because they have both deterministic and stochastic attributes. The deterministic attribute is based on the direct path and specular reflections: the direct path can be computed through geometrical raytracing as can specular reflections provided there is a map of the environment — hence the model name.

Since diffraction, which takes the lion's share of raytracing computation, can be neglected, raytracing can be made very efficient. The stochastic attribute of the model concerns the parameters of the clustered diffuse components, such as the K-factor and the angular spread.

A preliminary step in the reduction of channel models is clustering the paths extracted from the measurement data based on minimizing the multipath-component distance (MCD) in the delay-angle space. An underlying principle of our mmWave clustering algorithm in [13] is that each cluster contain only one specular reflection.[4] Figure 3 shows the paths extracted from a measurement campaign in a data center with our 60-GHz switched array. The paths were clustered in the delay-angle space: each cluster is represented by a different symbol and each path color-coded against path gain. The stronger path gain of the specular component is evident for most clusters. The sparsity of the channel, characterized by distinct clusters with narrow angular spreads ranging from 2°–4°, suggests that inter-beam interference will be minimal. There are nine clusters, hence up to nine separate streams for spatial multiplexing, leading to a variety of different MIMO implementations.

For example, consider a system using the 32-element phased array antennas in Fig. 2 with 3.6° beamwidth. The direct path (maroon circle) and the ceiling bounce (orange diamond) are the strongest paths and hence offer the highest SINR. Since the angular separation between the two paths (11°) exceeds the array beamwidth, the elements could be split into two subarrays, each forming a 7.2° beam aimed at the respective clusters. Another option is to split the array into four subarrays, each with a 14.4° beam; this option, however, would generate interference between the two clusters, so other clusters with wider angular separation, albeit lower SINR, could be selected. Yet another option is to aim the wider beam at the direct path but with a null on the ceiling bounce. Each channel response will offer different beamforming options.

Figure 4, instead, shows clustered paths in the delay-angle space from a measurement campaign in a hallway using our 60-GHz virtual array. In comparing clusters with the switched-array system, the delay tails are much longer for the virtual array — up to 16 ns compared to 6 ns for the switched array — because it can measure much greater path loss and hence can detect the weaker components as well. Also, only one path can be found per delay bin for the switched array, whereas up to three paths were found for the virtual array due to the much higher angular resolution.

In our measurements, we have found that the reflection loss for objects such as sheetrock walls and drop ceiling typically ranged between 6 dB–8 dB. The K-factor ranged between 5 dB–13 dB; equivalently, the percentage of the diffuse power with respect to the total cluster power ranged between 5–26 percent, but for some cases was measured as high as 40 percent. Indeed, the diffuse power interfering with the specular power can be significant and thus cannot be neglected for accurate channel modeling. Finally, the intra-cluster arrival rate — indicative of the delay

---

[4] However, it may occur that multiple specular paths originating from flat surfaces in close proximity are clustered together.

interval between paths within clusters — ranged from 1 GHz to 2 GHz. This parameter is important to know the number of paths that are expected within one radio sample.

MULTIPATH TRACKING

The beamforming training described earlier is divided into two stages: a coarse, exhaustive search over the 3D space of the RX and TX antennas followed by a refinement step in which the beams hone in on the exact path angle. In mobile environments, the angle will change as the transceivers or ambient reflectors move. Because the beamwidths are so narrow, misalignment of just a few degrees at both ends may incur an additional loss on the link budget of up to 30 dB [1]. Thus, to shorten training time, the coarse search can be skipped as long as the path angle changes gradually enough to be tracked through refinement only. Even if the beams maintain perfect alignment with a path, the path gain will vary due to different path lengths and different reflection angles as the beam traverses a scattering surface. How drastically the path gain changes is important for system design.

Figure 5 visualizes multipath tracking across 108 RX positions in a lecture room using our 60-GHz switched array system. The TX is labeled on the map of the environment, while the ground-truth (reported from robot) RX positions are marked with Xs. The dominant paths were tracked in the delay-angle space and then projected from the space onto the 2D map through inverse raytracing: the direct path was projected to the estimated position of the RX, while the reflected paths were projected to the estimated location of their reflection points. Each path is marked with a different symbol according to the legend and is color-coded against path gain. Since not all paths were detected across all positions, the beginning and end positions for each path are labeled. The three waypoints where the robot turned (positions 51, 70, and 95) are also labeled for reference.

One can see that the estimated direct path follows the ground-truth RX position very well. The path gain decreased as the robot moved farther from the TX and vice versa; its average deviation from the theoretical free-space value was 0.1 dB with a standard deviation of 1.5 dB. Now consider the right-wall track: For positions 1–51, the path gain increased continuously as the robot moved along the bottom segment of the loop until it achieved a maximum value around the first corner where the path length was shortest. From there, the path gain continued to decrease as the robot rounded the second corner, achieving a minimum value around the third corner, where the path length was longest; it then increased again until the final position in the loop. A mean reflection loss of 10.4 dB with a standard deviation of 4.2 dB over the track was observed. The behavior of the other three paths was similar.

DOPPLER SPREAD

Doppler frequency shift quantifies the rate of phase rotation (Eq. 1) due to movement of the transceivers or ambient reflectors. Per an earlier section, the shift depends on the center frequency and their relative velocity. Implicit in the relative velocity are relative speed and relative direction.
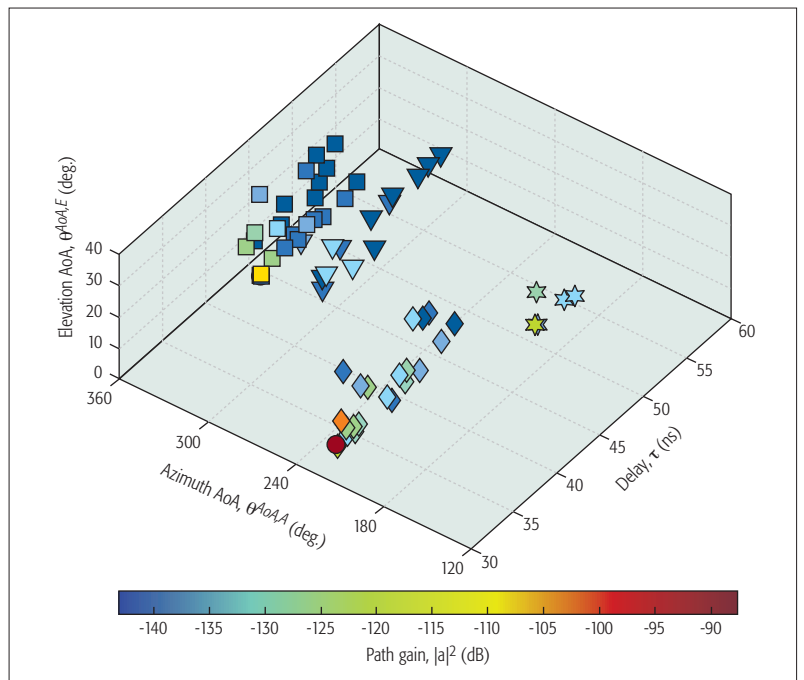

Figure 4. Power in the delay-azimuth-elevation space (AoA only) measured in a hallway with our 60-GHz virtual array. Each cluster is displayed with a different symbol, and each path is color-coded against path gain. Compared to the switched array, the delay tails of the clusters appear longer since the virtual array can also detect the weaker components arriving later.

The latter is captured through the double-directional angle of the direct path. In fact, each channel path — not only the direct path — will have a unique shift (Eq. 1). What differentiates their shifts is their angle only, not their relative speed since that is common to all paths.[5] This is substantiated in [14], where we show one-to-one correspondence between Doppler shift and angle of the channel paths using our 83-GHz switched-array system.

In the context of 5G, when transceivers steer their beams toward a dominant path, neighboring diffuse paths in the angle space will also be admitted based on how wide the beamwidth is. Each path admitted imparts a unique frequency shift that collectively results in a distorted frequency spectrum. The amount of distortion will depend on their relative path gains and relative frequency shifts (or equivalently relative angles given the one-to-one correspondence between the two) quantified through RMS Doppler spread, σ. Figure 6 displays the cumulative distribution function of the Doppler spread for eight dominant paths observed in a basement environment over 24 RX-TX configurations using our 83-GHz switched-array system [14]. The Doppler spread was computed for a 10° synthetic beamwidth, and the paths are ranked according to strength. The highest-ranked path ($j = 1$) corresponds to the direct path; since its angular spreads are within 0.5°, most Doppler spreads fall within 50 Hz. Even the lowest-ranked path ($j = 8$), associated with a weak reflection from a wall, has an angular spread up to 5°, but the Doppler spread does not exceed 700 Hz.

The channel coherence time is about 1.4 ms for $\sigma_{max} = 700$ Hz. While the Doppler spread did increase with beamwidth as more diffuse paths

---

[5] Assumes fixed ambient reflectors.

were admitted, we found this effect to be minor given the typical angular spreads mentioned earlier. If the beamwidth is increased enough, though, multiple dominant paths comparable in strength may also be admitted, giving rise to much higher Doppler spreads. Consequently, as for path loss models, so too should Doppler spread models be beamwidth dependent.

BLOCKAGE AND DEVICE-TO-DEVICE MODELS

Device-to-device models at mmWave will suffer from blockage from humans, vehicles, and so on given the low base station height. From our observations, as well as many others, the slow fading (shadowing) of human blockage will range between 20 dB–25 dB. While significant, the signal may still be recoverable for data transmission depending on the link budget. That is why, while the vast majority of papers only report on the slow fading, fast-fading characteristics of the blocked signal are also important, but still lacking in the literature, save one paper [15].

CONCLUSION

We have underscored some important aspects of channel models for mmWave systems: path loss models answer how far signals will propagate in an environment; dispersion models how many dominant paths are available and their distribution in space; multipath tracking models how the channel properties evolve in time; and Doppler models how the signal is distorted in the presence of mobility. We are currently working on models for fast fading during blockage events, and we plan to extend all models to outdoor environments.

REFERENCES

[1] Y. Wang et al., "28 GHz 5G-Based Phased-Arrays for UAV Detection and Automotive Traffic-Monitoring Radars," IEEE Radio Frequency Integrated Circuits Symp., June 2018.
[2] J. Senic et al., "Analysis of E-band Path Loss and Propagation Mechanisms in the Indoor Environment," IEEE Trans. Antennas and Propagation, vol. 65, no. 2, Dec. 2017, pp. 6562–73.
[3] IEEE 802.11ay Amendment; http://www.ieee802.org/11/Reports/tgay_update.htm.
[4] 5G mmWave Channel Model Alliance; https://www.nist.gov/ctl/5g-mmwave-channel-model-alliance/.
[5] F. Fuschini et al., "Item Level Characterization of mm-Wave Indoor Propagation," EURASIP J. Wireless Commun. and Networking, vol. 4, 2016.
[6] G. R. MacCartney, S. Deng, and T. S. Rappaport, "Indoor Office Plan Environment and Layout-Based MmWave Path Loss Models for 28 GHz and 73 GHz," IEEE VTC-Spring, May 2016.
[7] S. Hur et al., "Synchronous Channel Sounder Using Horn Antenna and Indoor Measurements on 28 GHz," IEEE Black Sea Conf., May 2014.
[8] D. Dupleich et al., "A Hybrid Polarimetric Wide-Band Beam-Former Architecture for 5G mm-Wave Communications," IEEE Wksp. Smart Antennas, Mar. 2016.
[9] R. Sun et al., "Design and Calibration of a Double-Directional 60 GHz Channel Sounder for Multipath Component Tracking," IEEE Euro. Conf. Antennas and Prop., Mar. 2017.
[10] A. Karttunen et al., "Spatially Consistent Street-by-Street Path Loss Model for 28-GHz Channels in Micro Cell Urban Environments," IEEE Trans. Wireless Commun., vol. 16, no. 11, Nov. 2017.
[11] S. Deng, G. R. MacCartney, and T. S. Rappaport, "Indoor and Outdoor 5G Diffraction Measurements and Models at 10, 20, and 26 GHz," Proc. IEEE GLOBECOM, Dec. 2016, pp. 1–7.
[12] A. Maltsev et al., "Quasi-Deterministic Approach to mmWave Channel Modeling in a Non-Stationary Environment," IEEE GLOBECOM, Dec. 2014.
[13] J. Wang et al., "Unsupervised Clustering for Millimeter-Wave Channel Propagation Modeling," IEEE VTC-Fall, Sept. 2017.
[14] J. Wang et al., "Quasi-Deterministic Model for Doppler Spread in Millimeter-Wave Communication Systems," IEEE Antennas and Wireless Propagation Letters, vol. 16, 2017, pp. 2195–98.
[15] M. Jacob et al., "Fundamental Analyses of 60 GHz Human Blockage," IEEE Euro. Conf. Antennas and Propagation, Apr. 2013.

Figure 5. Multipath tracking in a 19 m × 10 m lecture room. Five dominant paths were identified and labeled with different symbols according to the direct path or the object that generated the reflected path. The symbol at each RX position 1–108 is color-coded against path gain. For the direct path, the symbol lies at the estimated position of the RX (ground-truth position shown as X), while for the reflection paths, the symbol lies at the estimated location of the reflection points.

BIOGRAPHIES

CAMILLO GENTILE [M'01] received his B.S. and M.S. degrees from Drexel University in 1996 and his Ph.D. degree from Penn State University in 2001, all in electrical engineering. He joined the National Institute of Standards and Technology (NIST) in 2001. He has authored over 60 peer-reviewed papers and a book on geolocation techniques. In 2015, he became a project leader. His current interests include channel modeling and physical-layer modeling for millimeter-wave communication systems.
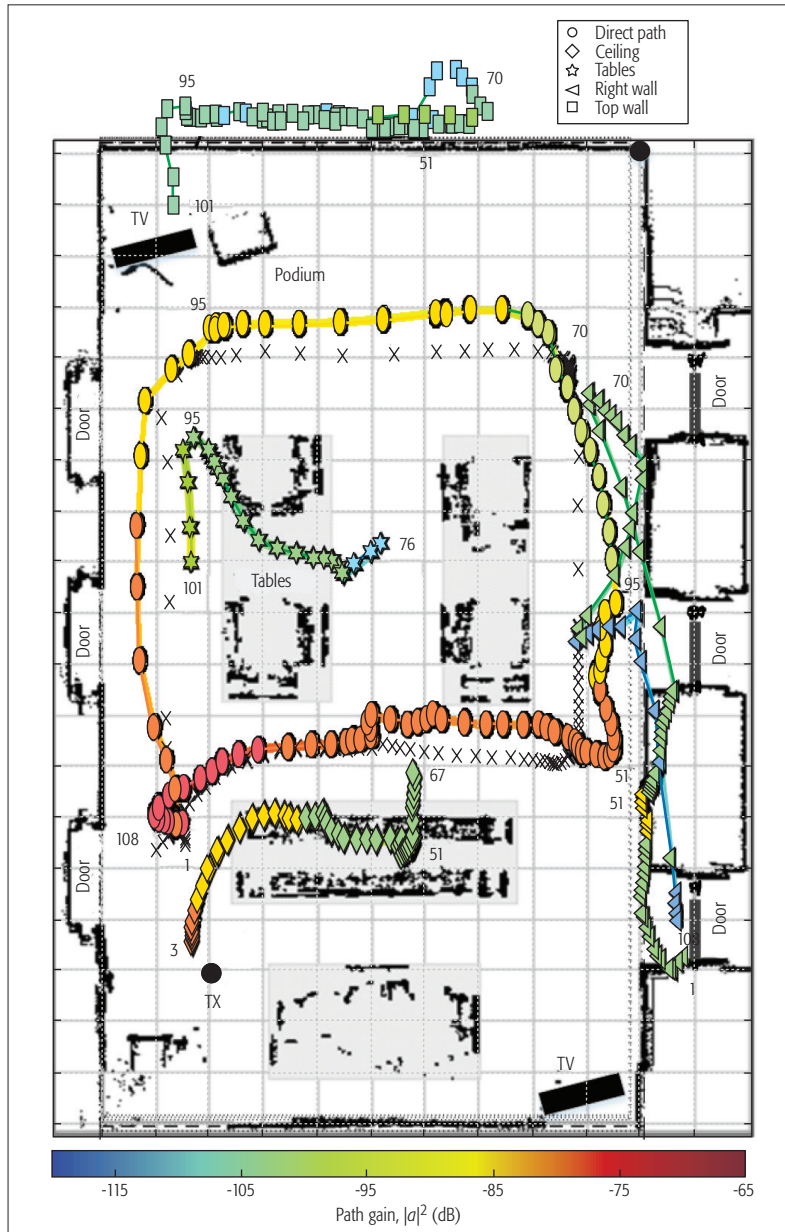
PETER PAPAZIAN [SM'98] received his B.S. in physics from State University of New York Stonybrook in 1973 and his M.S. degree from Colorado School of Mines in 1979. Currently, he is the 5G millimeter-wave Channel Sounder project leader at the NIST Communications Technology Laboratory, Boulder, Colorado. The purpose of this research is to conduct millimeter-wave radio channel propagation measurements to support model and standards development for 5G radio systems.

NADA GOLMIE received her Ph.D. in computer science from the University of Maryland at College Park. She is currently the chief of the wireless networks division in the Communications Technology Laboratory at NIST. Her research in media access control and protocols for wireless networks has led to over 100 technical papers presented at professional conferences and in journals. She serves as a Co-Chair for the 5G mmWave Channel Model Alliance.

KATE A. REMLEY is the leader of the Metrology for Wireless Systems Group at NIST, where her research includes improved calibrations and standardized measurements of microwave and millimeter-wave wireless systems. She received the Department of Commerce Bronze and Silver Medals and is a member of the Oregon State University Academy of Distinguished Engineers. She has chaired various MTT-S committees, was Editor-in-Chief of *IEEE Microwave Magazine*, and served as Distinguished Lecturer for the IEEE EMC Society.

PETER VOURAS received B.A. degrees in economics and foreign affairs from the University of Virginia, a B.S. degree in electrical and computer engineering from George Mason University, and an M.S.E. degree from Johns Hopkins University, Baltimore, Maryland. In 1996, he joined the Radar Division of the Naval Research Laborator,y and since October 2017 he has been with the Wireless Networks Division of NIST, Gaithersburg, Maryland.

JELENA SENIC received her B.S. and M.S. degrees in electrical engineering from the School of Electrical Engineering, University of Belgrade, Serbia, in 2009 and 2010, respectively. Since January 2015, she has been a guest researcher at NIST. Her current research interests include millimeter-wave communications, measurements of signal propagation, and channel modeling for 5G. The team in which she works received the Best Measurement Paper Award at EuCAP 2017.

JIAN WANG is with the Communication Technology Laboratory (CTL), NIST. Her research interests include next generation wireless communications and public safety communications. Before joining NIST, she worked in the wireless industry on digital signal processing and wireless protocol development. She received her B.S. degree in electrical engineering from Tongji University, Shanghai, China, and her M.S. degree in electrical engineering from Washington State University.
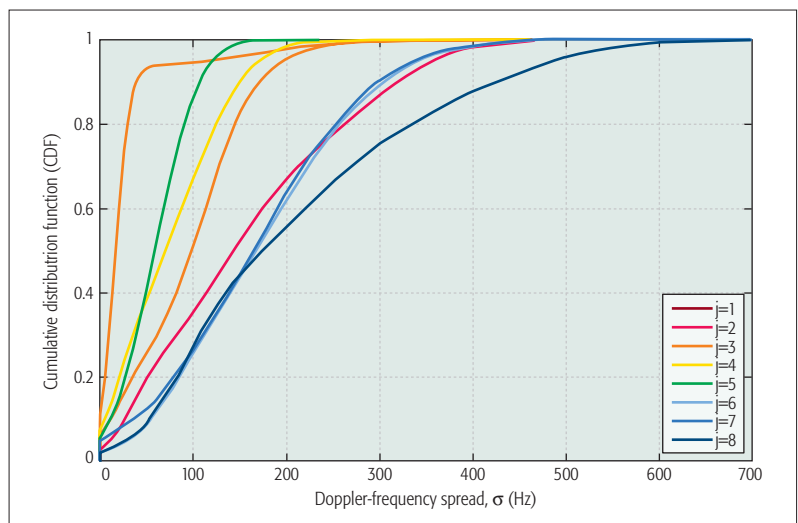

Figure 6. Cumulative distribution function of the Doppler spread for eight dominant paths observed in a basement environment using our 83-GHz switched array system. The Doppler spread is based on a 10° beamwidth, and the paths are ranked according to strength.

DEREK CAUDILL received a B.S. degree in electrical engineering and an M.S. degree in electrical and computer engineering from the University of Massachusetts Amherst in 2016 and 2017, respectively. As a research associate within the CTL at NIST, he supports the data acquisition efforts of mmWave channel model measurements and the systems on which such measurements depend.

RUOYU SUN [M'13, SM'17] received his B.S. degree from Tianjin University in 2004, his M.S. degree from Beijing Jiaotong University in 2007, and his Ph.D. degree from the University of South Carolina in 2015, all in electrical engineering. He is a lead architect at CableLabs, Louisville, Colorado. He was an electronics engineer at NIST. His research interests include radio propagation channel measurements and modeling.

JACK CHUANG was a graduate research assistant in the Communications and Space Sciences Laboratory (CSSL) at the Pennsylvania State University and obtained his Ph.D. degree in 2008. He then worked at BAE Systems in electronic warfare and at Cisco Systems in spectrum sharing. He is currently with NIST Communication Technology Lab, Gaithersburg, Maryland,, developing 5G mmWave channel sounders.